Flaw size-dependent mechanical interlayer coupling and edge-reconstruction embrittlement in van der Waals materials

Zhigong Song[1,2,†], Boyu Zhang[1,†], Yingchao Yang[1,3,†], Guanhui Gao[1], Daiming Tang[4,5], Qiyi Fang[1], Youtian Zhang[1], Bongki Shin[1], Doug Steinbach[1], Qing Ai[1], Xuan Zhao[6,7], Yimo Han[1], Nitin P. Padture[8], Brian Sheldon[8], Takashi Taniguchi[9], Kenji Watanabe[10], Huajian Gao[11,2,8,*] and Jun Lou[1,*]

Affiliations:

[1] Department of Materials Science and NanoEngineering, Rice University, 6100 Main Street, Houston, TX 77005, USA

[2] Institute of High Performance Computing (IHPC), Agency for Science, Technology and Research (A*STAR), 1 Fusionopolis Way, #16-16 Connexis, Singapore 138632, Singapore

[3] Department of Mechanical and Aerospace Engineering, University of Missouri, 416 S. 6th St. , Columbia, MO 65211, USA

[4] International Center for Materials Nanoarchitectonics, National Institute for Materials Science, 1-1 Namiki Tsukuba Ibaraki 305-0044, Japan.

[5] Institute of Pure and Applied Sciences, University of Tsukuba, Tsukuba, 305-8571 Japan

[6] Department of Electrical and Computer Engineering, Rice University, Houston, TX 77005, USA

[7] Applied Physics Graduate Program, Smalley-Curl Institute, Rice University, Houston, TX 77005, USA

[8] School of Engineering, Brown University, 184 Hope Street, Providence, RI 02912, USA

[9] Research Center for Materials Nanoarchitectonics, National Institute for Materials Science, 1-1 Namiki Tsukuba Ibaraki 305-0044, Japan.

[10] Research Center for Electronic and Optical Materials, National Institute for Materials Science, 1-1 Namiki Tsukuba Ibaraki 305-0044, Japan.

[11] School of Mechanical and Aerospace Engineering, Nanyang Technological University (NTU), 50 Nanyang Avenue, Singapore 639798, Singapore

*Corresponding Author: gao.huajian@tsinghua.edu.cn (H. Gao) and jlou@rice.edu (J. Lou)

[†] These authors contributed equally

Abstract

Van der Waals (vdW) materials with strong in-plane covalent bonding and weak interlayer interactions consist of two-dimensional (2D) building blocks such as graphene and monolayer hexagonal boron nitride (*h*-BN). These multilayer 2D materials exhibit exceptional mechanical characteristics, showcasing impressive fracture resistance as demonstrated in monolayer *h*−BN. Nonetheless, preserving these remarkable fracture properties in vdW materials remains a challenge. Here we reveal an anomalous mechanical interlayer coupling that involves interlayer-friction toughening and edge-reconstruction embrittlement during the fracture of multilayer *h*-BN. Both asynchronous and synchronous fracture modes and their flaw-size dependence are identified. Edge reconstruction in the synchronous fracture mode can eliminate a lattice asymmetry induced toughening mechanism in monolayer *h*-BN leading to embrittlement of the multilayer *h*-BN, while the asynchronous fracture mode results in greater fracture resistance. Such findings will provide fundamental guidelines for engineering interlayer interactions in vdW materials including heterostructures and layered architectures for better mechanical and functional performances.

Main Text

Pristine monolayer two-dimensional (2D) materials have been attracting worldwide attention over the last two decades owing to their exceptional properties. The relatively weak van der Waals (vdW) interlayer interactions and the ultrahigh surface-to-volume ratio of monolayers, allow assembly of monolayers with the same or different chemical compositions into multilayer structures, opening up the whole new field of vdW materials. Many exotic behaviors have been demonstrated in these multilayer structures, such as unconventional superconductivity in bilayer graphene at a magic twisting angle [1], super-lubricity through incommensurate contacts between 2D layers [2-4], formation of moiré excitons that can resonantly couple with phonons, and interlayer p-n junction as well as interlayer tunneling effects [5-8]. These interesting interlayer coupling behaviors are thought to be activated by tailoring the stacking order (AA', AB, etc.), stacking sequence (graphene/*h*-BN, MoS_2/graphene, etc.), and twisting angle, which inspires fundamentally new approaches to device engineering [1,9-11]. Despite this exciting progress, studies on the effects of interlayer coupling on the overall mechanical performance, especially fracture behavior, of multilayer structures are still in a nascent stage.

The emerging vdW materials with strong in-plane covalent bonding and weak interlayer interactions can be constructed from diverse 2D building blocks, and it is well known that these 2D building blocks in their monolayer forms exhibit exceptional mechanical properties such as ultrahigh strength [12,13]. However, for many practical uses of various vdW materials including heterostructures and layered architectures, retaining outstanding mechanical properties of monolayers in their multilayer structures remains a major challenge. One famous example is the strong and stiff graphene versus the relatively weak and soft graphite. The lack of strong interlayer interaction is generally believed to be the main contributing factor for such a challenge. Therefore, understanding, and more importantly, developing corresponding strategies to maintain high strength and fracture resistance of 2D materials from monolayer to multilayer vdW materials becomes a very important topic to be explored.

It is currently hypothesized that interlayer friction could increase the toughness of multilayer structures when compared to their monolayer counterparts by retarding both crack initiation and propagation. This toughening effect has been successfully demonstrated in both multilayer graphene and MoS_2 systems [14,15]. For example, the strength and elastic modulus of monolayer graphene is as high as 130 GPa and 1 TPa [12], respectively. The fracture toughness of monolayer graphene however, is only 4 $MPa.m^{1/2}$ [16], while multilayer graphene's fracture toughness can reach as high as 8.65±0.46 $MPa.m^{1/2}$ due to interlayer-friction toughening [14].

Multilayer *h*-BN (MBN) is an exciting material to study the multilayer effects on fracture behaviors due to the unique fracture behavior of single layer *h*-BN (SBN). Like graphene, SBN has a 2D hexagonal lattice, albeit with alternating boron (B) and nitrogen (N) atoms instead of all carbon (C) atoms, an ultrahigh strength (~100 GPa) and an ultrahigh elastic modulus (~0.8 TPa) [13]. As the toughest monolayer 2D material verified by both experimental observations and theoretical predictions, SBN is shown to be intrinsically tough due to its asymmetric lattice structure. This asymmetric lattice structure exhibits repeated occurrences of crack deflection and branching along the crack path [13]. Due to the atomic polarity between B and N atoms, thermodynamically stable MBN generally prefers the AA' stacking order, unlike multilayer graphene which is in the AB stacking order [17]. MBN has been shown to maintain the superior strength and elastic modulus from its monolayer constituent [18], SBN, but there have been very few quantitative experimental studies on the fracture behaviors of MBN in AA' stacking order. Earlier fracture studies on MBN with disordered stacking demonstrated that the fracture properties of MBN do not directly benefit from the effects of interlayer friction or intralayer lattice asymmetry [19].

In this work, we investigated the fracture behaviors of MBN. We observed two fracture modes, controlled by the initial flaw size, in AA'-stacked MBN through quantitative *in-situ* measurements and systematic multiscale mechanics analyses. Depending on the initial flaw size, AA' MBN exhibited either a toughening effect due to interlayer friction and intralayer lattice asymmetry, or an embrittlement effect due to interlayer B-N bond formation. This understanding of MBN fracture could provide important guidance on engineering the interlayer mechanical coupling in MBN and other vdW materials. In a broader sense, the intriguing structure-property relationship unveiled in this work could also contribute to new design principles of layered architectures as already successfully demonstrated in nacre [20,21] and lamella structures [22,23].

Results

MBN in AA' stacking order was prepared using the mechanical exfoliation method. Details can be found in **Supplementary Section 1**. A high-quality bulk single crystal *h*-BN was exfoliated several times and then transferred to a silicon wafer. MBN samples were then carefully examined under an optical microscope. Samples with the proper size, shape, and thickness, of around 10 nm, were subsequently dry transferred to the Rice push-to-pull (PTP) mechanical testing devices. The Rice PTP device converts a compressive force on the device to an in-plane tensile force on a sample. A nanoindenter inside the scanning electron microscope (SEM) was used to actuate the PTP devices. To measure the sample strain precisely, Pt fiducial markers were deposited on the sample surface for digital image correlation (DIC) analyses, as indicated in **Fig. 1**. Three representative *in situ* tensile tests of MBN samples were selected to demonstrate the intrinsic fracture behaviors of MBN. **Fig. 1** (**a**) and (**b**) show the in-plane tensile test of Sample #1 (MBN ribbon with suspended length L = 2.354 µm, suspended width W = 2.804 µm, and thickness t = 8 nm). The tensile strength and failure strain of Sample #1 is ~9.48 GPa and ~1.81%, respectively. As observed in **Fig.1** (**b**), Sample #1 fractured asymmetrically with cracks deflecting and branching along the rough crack path, which is commonly seen in its monolayer component, SBN [13]. To measure the fracture toughness and more closely observe the intrinsic fracture behavior of MBN, a central pre-crack with a specific length (2a) was cut with a focus ion beam (FIB) in Sample #2 and #3, as shown in **Fig. 1** (**c**) and (**e**).

The dimensions of Sample #2 are L = 2.6 µm, W = 5.36 µm, and t = 10 nm with a central pre-crack (2a ~ 0.847 µm), as shown in **Fig. 1** (**c**) and (**d**). The tensile strength and failure strain of Sample #2 is ~8.96 GPa and ~1.3%, respectively, which are very close to the strength and failure strain of Sample #1. Interestingly, the crack path leading to final fracture completely bypassed the central pre-crack and the crack morphology was rough, similar to the crack morphology observed in MBN without a pre-crack in **Fig. 1** (**b**). Such flaw insensitive (FI) behavior is quite unexpected in a multilayer 2D material system. According to the Chen and Gao model for FI behavior [24], the width of Sample #2 falls into the range of FI due to the ultrahigh fracture toughness of SBN and possible interlayer-friction toughening in MBN. More detailed analyses and derivations are presented in the **Supplementary Section 2** and **3**. Owing to the interlayer-friction toughening effect, the critical energy release rate (J_C) of MBN should be no less than twice of SBN's, i.e. 172.7 J/m^2, and the critical SIF (K_C) of MBN is no less than 11.8 MPa.m$^{1/2}$ accordingly. The failure of MBN is strength-dominated, and rough fracture surfaces are present owing to the asymmetrical fracture behaviors.

However, as seen in **Fig. 1** (**e**) and (**f**), an interesting fracture mode of Sample #3, which differed significantly from Sample #2, is unveiled. The size of Sample #3, L = 2.742 µm, W = 5.064 µm, and t = 9 nm, is similar to Sample #2, but it has a longer pre-crack length of 2a = 1.65 µm. In this case, ideal brittle fracture behavior with a straight crack path and clean cleavage were captured, which is totally different from both SBN [13], and Samples #1 and #2. According to the **Supplementary Table S1**, we further categorize the test results into three groups: MBN with no pre-crack, MBN with a short pre-crack ($2a < 0.85$ μm), and a long pre-crack ($2a > 1.2$ μm). The summarized failure strengths (solid lines) and predicted limiting strengths (dashed lines) are shown in **Fig. 1** (**g**). The failure strength of MBN with a short pre-crack is 7.62±0.94 GPa, which is close to that of MBN with no pre-crack 7.67±1.41 GPa. Interestingly, the value is even a little higher than its predicted FI strength (6.59 GPa), which indicates the limiting strength with FI behaviors as predicted in **Supplementary Section 3**. However, the failure strength of MBN with a long pre-crack dropped drastically to 1.91±0.19 GPa, compared to the predicted FI strength 5.38 GPa, implying an entirely different failure mode. Furthermore, the calculated critical stress intensity factor (SIF) of Sample #3 surprisingly dropped to $K_{IC} = 1.98$ MPa.m$^{1/2}$, which is unexpected based on previous findings in SBN [13], and also contradictory to the prediction of Griffith relation ~3.3 MPa.m$^{1/2}$ [13,25]. These interesting but somewhat contradictory observations imply that flaw size in MBN plays an important role in triggering significant changes in the fracture behavior of this multilayer system.

To reveal the underlying role played by flaw size in the fracture of MBN, three typical samples with pre-crack lengths of $2a$ = ~0.8 μm, 1.2 μm and 1.4 μm are shown in **Fig. 2**. As shown in **Fig. 2** (**a**), the failure strength and strain is reduced with increasing pre-crack length as expected, but the measured critical SIF (K_{IC}) counterintuitively shows the same trend which normally should be independent of pre-crack length [13,26,27]. To better observe the fracture edge morphology and understand the underlying fracture mechanisms, TEM characterization was carefully performed on fractured MBN samples. PTP devices with fractured samples were directly loaded into the TEM to avoid any potential damage to the fracture edges. Crack deflections were clearly observed in samples with short pre-crack length, as shown in **Fig. 2** (**b**) and **(c**), which is consistent with the asymmetric fracture characteristics of SBN [13]. The characteristics of asynchronous fracture featuring stair-case edges are shown in **Fig. 2** (**c**), which is commonly seen in AB stacked multilayer 2D systems [14,15]. The rough fracture edges were clearly observed at both the micro- and nanometer length scales. To highlight asynchronously fractured layers with rough fracture edges, the TEM image is colored-coded based on contrast difference as shown in **Fig. 2** (**c**). As the flaw size (pre-crack length) in MBN increases**,** the asynchronous fracture behavior fades away at the micrometer scale and no stair-case crack edges are observed from SEM images as shown in **Fig. 2** (**d**). However, from the

TEM image shown in **Fig. 2** (**e**), rough fracture edges and stair-case crack edges still exist at the nanometer scale, indicating that asynchronous fracture persists to a limited extent. Therefore, the asynchronous fracture behavior, represented in the form of the average spacing between crack edges of different layers, diminishes from several hundreds of nanometers to a few nanometers, as shown in **Fig. 2** (**d**) and (**e**). The asynchronous fracture mode is further suppressed with the increase of the pre-crack length. As shown in **Fig. 2** (**f**) and (**g**), atomically smooth fracture edges were observed at both the micro- and nanometer length scales. A distinguishing feature observed is a straight dark line, which is consistent with the characterization of closed edges of multilayer 2D materials [28,29]. The insert in **Fig. 2** (**g**) shows the closed edge structures. According to the TEM simulations, it is reasonable to have a darker contrast for the closed edges due to the higher local atomic density. Details can be found in **Supplementary Section 1**. It can be inferred that only simultaneous fracture along the same crack path in different layers could result in such uniform and smooth fracture edges as shown in **Fig. 2** (**g**), demonstrating a very intriguing synchronous fracture process.

To confirm this highly interesting flaw-size dependent fracture behavior, a series of tests on MBN samples with different pre-crack lengths were conducted. A summary of the measured or estimated (in flaw-insensitive cases) fracture toughness data as a function of the pre-crack length was listed in **Supplementary Table S1**. Samples with FI fracture behaviors were commonly found when pre-crack length was below 0.85 µm. With the increase of the pre-crack length, the FI fracture behaviors became absent, and the average fracture toughness quickly decreases to ~2 MPa.m$^{1/2}$. Meanwhile, the fracture modes of MBN were observed to transition from asynchronous to synchronous fracture.

Based on *in situ* quantitative fracture tests and high-quality SEM and TEM images, it is clearly seen that there exist two very different fracture modes in MBN: asynchronous fracture *vs*. synchronous fracture. Asynchronous fracture mode (fracture occurs along different crack paths in each layer) generally leads to a higher fracture resistance and rough (staircase) fracture edges, while synchronous fracture mode (fracture appears to occur along a common crack path in each layer) leads to a reduced fracture resistance and ultra-smooth fracture edges. It appears that the initial flaw (pre-crack) size in MBN plays an important role in determining the transition between these two fracture modes (**Fig. 2**), but the physical origin and underlying mechanisms remain elusive. Therefore, multiscale mechanics analyses were performed to understand the structural origins of dual fracture modes in MBN and to explore the underlying mechanisms associated with the observed flaw-size dependent fracture behaviors.

The unique AA’ stacking order of MBN makes it, under certain circumstances, favor synchronous fracture because of the possible formation of interlayer B-N bonds on fracture edges of adjacent layers leading to straight and closed edges. To get a complete picture of such behavior, we analyzed two distinctive fracture processes in MBN: (**I**) intralayer B-N bond breakage without interlayer B-N bond formation; (**II**) intralayer B-N bond breakage with interlayer B-N bond formation. In fracture process (**II**), the interlayer B-N bond formation leads to edge reconstruction. Fully reconstructed edges can have two possible patterns of bi-planar edge reconstruction — type I edge reconstruction and type II edge reconstruction — both of which are studied carefully (**Fig. 3**).

A multiscale mechanics analysis under ideal K_{I} loading field is carried out to investigate the intrinsic fracture behaviors of MBN during the crack growth initiation stage as shown in **Fig. 3** (**a**). The yellow region is modelled by the *ab initio* method to accurately capture the atomic reconstruction in the fracture processing zone. The J integral in **Fig. 3** (**b-e**) is only an evaluation of local loading to record the corresponding critical events at crack tip, but not a prediction for energy release rate, considering the lattice trapping effect [30]. Detailed descriptions of the analysis are presented in the **Supplementary Section 4**. The accurate J_C and K_C of MBN under the fracture process (**I**) and (**II**) follows the analyses in the **Supplementary Section 2** and **5**. Following the fracture process (**I**), if none of the fractured edges behind the crack tip are reconstructed, the interlayer interactions of MBN are dominated by interlayer friction, which shows strong asynchronous characteristics due to the lack of out-of-plane mirror symmetry in MBN. As shown in **Fig. 3** (**b**), the crack tip bifurcates when J = 13.0 J/m^2, close to that of SBN, which bifurcates at J = 11.5 J/m^2 [13]. Then the bifurcated tip fails at J_C = 17.5 J/m^2, featuring an asynchronous characteristic — cracks on adjacent layers deflect in different directions. Following the fracture process (**II**), if interlayer B-N bonds at fractured edges behind the crack trip are formed and lead to edge reconstruction, the formation of interlayer bond will dominate the interlayer interaction of MBN, which results in synchronous fracture because edge reconstruction stitches the two exposed fractured edges together into a folded structure thereby reducing the fracture energy. According to the Griffith relation, the accurate J_C and K_C of MBN with complete edge reconstruction can be obtained by evaluating the formation energy of MBN’s folding structure in unit length, J_C = ~3.80 J/m^2 and K_C = ~1.75 MPa.m$^{1/2}$ (See **Supplementary Section 5**). The fracture of MBN in process (**II**) is synchronous across adjacent layers, leading to brittle fracture with a lower fracture toughness as observed experimentally. More details about crack growth in adjacent layers can be found in **Fig. 3** (**d**) and (**e**). **Fig. 3** (**d**) presents typical asynchronous fracture behaviors. Once the crack initiates, crack bifurcation and repeated deflection occur in different directions of adjacent layers due to the lack of both in-plane and out-of-plane mirror symmetry in MBN as shown in **Fig. 3** (**d**). MBN with asynchronous fracture demonstrates higher fracture toughness than SBN due to the interlayer-friction shielding effect [13]. **Fig. 3** (**e**) presents typical synchronous fracture behaviors. The crack grows straight in-plane with edge reconstructions following the crack tip. Interestingly, benefitting from the unique AA' stacking order, there can be two possible types of edge reconstruction in MBN as shown in **Fig. 3** (**f**) and (**g**). For type I edge reconstruction, interlayer B-N bond formation occurs between the same two layers on both side of the crack; while for type II edge reconstruction, individual layers form interlayer B-N bond with a different layer on each side of the crack. In both cases, the crack tip advances in a typical brittle manner and leaves a straight crack path. In the synchronous fracture mode, no dangling bond is formed from crack propagation, and the MBN exhibits a much lower fracture toughness than SBN [13]. In other words, the in-plane lattice asymmetric toughening mechanism that made SBN the toughest 2D material [13] can be diminished in MBN due to edge reconstructions following the crack tip.

Based on our experimental observations of the flaw-size dependent fracture behaviors in MBN, it is reasonable to assume that the formation of out-of-plane B-N bonds in edge reconstructions is also flaw-size dependent. Here, two models are formulated to comprehend this flaw-size dependence employing multiscale mechanics analyses as shown in **Fig. 4** (**a**). In **Fig. 4** (**a**), the MBN sample under uniaxial tension along the *y* direction is prepared with a central pre-crack along the *x* direction. The in-plane boundary of the continuum region is defined by the analytical solution of the displacement field containing a central pre-crack under uniaxial loading [31]. The out-of-plane boundary is periodic. Detailed settings of the model are presented in the **Supplementary Section 6**.

The first model is to unveil the relationship between the mobility of the reconstructed crack tip and the flaw size in MBN, as illustrated in **Fig. 4** (**b**). When a reconstructed crack tip advances lattice by lattice, no dangling bond could be formed, and the translational symmetry is preserved. Therefore, based on this feature, a stress-augmented activation model is proposed to clarify the relationship between the mobility of the reconstructed crack tip and the flaw size in MBN under critical loading [32,33]. The flaw size is obtained from the measured pre-crack length of MBN samples tested via *in situ* tensile experiments. The MBN samples with varying flaw sizes are then categorized into two groups: failure with FI behaviors (denoted as FI and colored red) and failure without FI behaviors (denoted as non-FI and colored blue). The flaw-size dependence of fracture behaviors can be extracted from the predicted mobility of the reconstructed crack tip. Detailed derivations can be found in the **Supplementary Section 7**. As shown in **Fig. 4** (**c**), it is obvious that the propagation of the reconstructed crack tip will be more favorable as the flaw size grows longer. When the flaw size is smaller than 0.8 μm, the mobility of reconstructed crack tip is reduced to less than 1×10^{-10} nm/s, which is unlikely to be detected under normal conditions, implying that the reconstructed crack tip can hardly propagate owing to the suppressed edge reconstruction. As the flaw size grows larger than 1.0 μm, the mobility of reconstructed crack tip is significantly increased according to the stress-augmented activation model, eventually giving rise to the synchronous fracture mode.

The second model is to explore the relation between the energy landscape in edge reconstruction and the flaw size in MBN. As shown in **Fig. 4** (**b**), the edge reconstruction in MBN can be decomposed into two events, intralayer cleavage and interlayer healing. The intralayer cleavage is denoted as the breakage of the B^1-N^1 bond and the N^2-B^2 bond, and the interlayer healing is the formation of the B^1-N^2 bond and the B^2-N^1 bond. The energy consumed by intralayer cleavage is a constant, theoretically twice of the B-N bond formation energy in a bilayer *h*-BN model, none of which is dependent on flaw-size. Meanwhile the energy barrier of interlayer healing, the final event in edge reconstruction shown in **Fig. 4** (**d**), varies due to the intralayer and interlayer interatomic distance, which is affected by the in-plane flaw-size dependent boundary conditions. Therefore, to explore the flaw-size dependent energy landscape of edge reconstruction is to quantify the relationship between the energy barrier of the interlayer healing and the flaw size. The energy barrier can serve as a measure of the capability for the edge reconstruction to follow the crack tip closely during crack propagation, which is a suitable criterion to predict whether the crack propagation is synchronous or asynchronous. Obviously, an easy-to-overcome energy barrier will allow edge reconstruction to keep up with the crack tip lattice by lattice and lead to a synchronous fracture under critical loading. The basic setting for calculating the reconstructed energy barrier is based on the MBN model with a central pre-crack in **Fig.4** (**a**). By changing the central pre-crack length and extracting the reconstructed energy barrier, the flaw-size dependence of the reconstructed energy barrier could be assessed. Usually, a volume change, due to atomic reconstruction while investigating the energy barrier of a phase transition in a finite cell composed of several atoms, could complicate the results severely. Therefore, the generalized solid-state nudged elastic band (G-SSNEB) method, which is widely adopted in exploring the energy barrier of phase transitions in a small system [34], is utilized in the *ab initio* modeling to comprehensively evaluate the atomic reconstruction aligned with the corresponding cell volume change in the z dimension (out-of-plane direction with periodic boundary condition). Details can be found in **Supplementary Section 8.** Clear flaw-size dependence of the energy barrier ΔE_b in interlayer healing is shown in **Fig. 4** (**e**), no matter which type of edge reconstruction occurs as indicated in **Fig. 4** (**d**). The ΔE_b decreases with increasing flaw size, indicating that edge reconstruction occurs much more easily in the presence of a longer pre-crack, which confirms the unique flaw-size dependent dual fracture behaviors observed in MBN. Due to the experimental challenges of directly observing the interlayer bond formation in our samples, the proposed interlayer bonding in the synchronized fracture mode remains to be verified by experiments.

Conclusion

It is of significant importance to understand how to preserve outstanding properties of monolayer constituents in multilayer assemblies. The fascinating fracture behaviors of SBN and the unique structure of MBN provide an ideal test bed for exploring the influence of interlayer mechanical coupling on the fracture behaviors of multilayer nanomaterials. In MBN, interlayer friction associated with the vdW interaction can be treated as a type of weak interlayer mechanical coupling, which can lead to flaw-insensitive and asynchronous fracture behaviors. On the other hand, activated by out-of-plane B-N bond formation at the fractured edges in adjacent layers, strong interlayer mechanical coupling enabled by edge reconstructions could result in flaw-sensitive and synchronous fracture behaviors. By increasing the pre-crack (flaw) size in MBN, the transition from asynchronous fracture to synchronous fracture was observed experimentally and explained by multiscale mechanics analyses. With the rise of vdW solids or 2.5D materials [35], solid materials and structures constructed by engineering interlayer interactions represent an important paradigm shift in designing novel materials for many exciting applications [4,36-38]. The findings from this study represent a solid step forward towards designing and engineering more robust vdW materials against fracture and inspiring the optimal design of layered architectures.

Acknowledgments

The authors gratefully acknowledge the financial support by the US Department of Energy, Office of Basic Energy Sciences under Grant Number DE-SC0018193. H.G. acknowledges a start-up grant from Nanyang Technological University (002479-00001) and Agency for

Science, Technology and Research (A*STAR). During the revision of this manuscript, the affiliation of Prof. Huajian Gao has changed to Mechano-X Institute, Applied Mechanics Laboratory, Department of Engineering Mechanics, Tsinghua University, Beijing 100084, China.

Author Contributions

Z. S., B. Z. and Y. Y. conceived the project. B. Z., Y. Y. and J. L. designed the experiments and analyzed the data. Z. S. and H. G. performed simulations and analyzed the results. G. G., Y. H. and D. T. performed TEM analysis. Q. F., B. Shin., D. S., Q. A. and X. Z. helped with the sample preparation and characterization. Y. Z. performed digital image correlation. T. T. and K. W. performed material synthesis. Z. S. B. Z. Y.Y. supervised by N. P., B. Sheldon., J. L. and H. G. drafted the manuscript with inputs, discussion, and approval from all co-authors. Z. S., B. Z. and Y.Y. contributed equally to this work.

Competing Interests

The authors declare no competing interests.

References

1 Cao, Y. *et al.* Unconventional superconductivity in magic-angle graphene superlattices. *Nature* **556**, 43-50 (2018).

2 Liu, Z. *et al.* Observation of microscale superlubricity in graphite. *Physical Review Letters* **108**, 205503 (2012).

3 Liao, M. *et al.* UItra-low friction and edge-pinning effect in large-lattice-mismatch van der Waals heterostructures. *Nature Materials* **21**, 47-53, (2022).

4 Song, Y. *et al.* Robust microscale superlubricity in graphite/hexagonal boron nitride layered heterojunctions. *Nature Materials* **17**, 894-899, (2018).

5 Jin, C. *et al.* Observation of moiré excitons in WSe_2/WS_2 heterostructure superlattices. *Nature* **567**, 76-80, (2019).

6 Shinokita, K., Miyauchi, Y., Watanabe, K., Taniguchi, T. & Matsuda, K. Resonant Coupling of a Moiré Exciton to a Phonon in a $WSe_2/MoSe_2$ Heterobilayer. *Nano Letters* **21**, 5938-5944, (2021).

7 Nakamura, K. *et al.* All 2D Heterostructure Tunnel Field-Effect Transistors: Impact of Band Alignment and Heterointerface Quality. *ACS Applied Materials & Interfaces* **12**, 51598-51606, (2020).

8 Sukma Aji, A. *et al.* Two-step synthesis and characterization of vertically stacked SnS–WS_2 and SnS–MoS_2 p–n heterojunctions. *Physical Chemistry Chemical Physics* **20**, 889-897, (2018).

9 Park, J. M. *et al.* Robust superconductivity in magic-angle multilayer graphene family. *Nature Materials* **21**, 877-883, (2022).

10 Ribeiro-Palau, R. *et al.* Twistable electronics with dynamically rotatable heterostructures. *Science* **361**, 690-693, (2018).

11 Kapfer, M. *et al.* Programming twist angle and strain profiles in 2D materials. *Science* **381**, 677-681, (2023).

12 Lee, C., Wei, X., Kysar, J. W. & Hone, J. Measurement of the elastic properties and intrinsic strength of monolayer graphene. *Science* **321**, 385-388 (2008).

13 Yang, Y. *et al.* Intrinsic toughening and stable crack propagation in hexagonal boron nitride. *Nature* **594**, 57-61 (2021).

14 Jang, B. *et al.* Asynchronous cracking with dissimilar paths in multilayer graphene. *Nanoscale* **9**, 17325-17333, (2017).

15 Jung, G. S. *et al.* Interlocking Friction Governs the Mechanical Fracture of Bilayer MoS2. *ACS Nano* **12**, 3600-3608, (2018).

16 Zhang, P. *et al.* Fracture toughness of graphene. *Nature Communications* **5**, 1-7 (2014).

17 Constantinescu, G., Kuc, A. & Heine, T. Stacking in Bulk and Bilayer Hexagonal Boron Nitride. *Physical Review Letters* **111**, 036104, (2013).

18 Falin, A. *et al.* Mechanical properties of atomically thin boron nitride and the role of interlayer interactions. *Nature Communications* **8**, 15815, (2017).

19 Wei, X. *et al.* Comparative Fracture Toughness of Multilayer Graphenes and Boronitrenes. *Nano Letters* **15**, 689-694, (2015).

20 Aksay, I. A. *et al.* Biomimetic Pathways for Assembling Inorganic Thin Films. *Science* **273**, 892-898, (1996).

21 Finnemore, A. *et al.* Biomimetic layer-by-layer assembly of artificial nacre. *Nature Communications* **3**, 966, (2012).

22 Wu, X. *et al.* Heterogeneous lamella structure unites ultrafine-grain strength with coarse-grain ductility. *Proceedings of the National Academy of Sciences* **112**, 14501-14505, (2015).

23 Wegst, U. G. K., Bai, H., Saiz, E., Tomsia, A. P. & Ritchie, R. O. Bioinspired structural materials. *Nature Materials* **14**, 23-36, (2015).

24 Gao, H. & Chen, S. Flaw Tolerance in a Thin Strip Under Tension. *Journal of Applied Mechanics* **72**, 732-737, (2005).

25 Griffith, A. A. VI. The phenomena of rupture and flow in solids. *Philosophical transactions of the royal society of london. Series A, containing papers of a mathematical or physical character* **221**, 163-198 (1921).

26 Buehler, M. J. & Gao, H. Dynamical fracture instabilities due to local hyperelasticity at crack tips. *Nature* **439**, 307-310 (2006).

27 Buehler, M. J., Abraham, F. F. & Gao, H. Hyperelasticity governs dynamic fracture at a critical length scale. *Nature* **426**, 141-146 (2003).

28 Liu, Z., Suenaga, K., Harris, P. J. F. & Iijima, S. Open and Closed Edges of Graphene Layers. *Physical Review Letters* **102**, 015501, (2009).

29 Alem, N. *et al.* Subangstrom Edge Relaxations Probed by Electron Microscopy in Hexagonal Boron Nitride. *Physical Review Letters* **109**, 205502, (2012).

30 Thomson, R., Hsieh, C. & Rana, V. Lattice trapping of fracture cracks. *Journal of Applied Physics* **42**, 3154-3160 (1971).

31 Weertman, J. Dislocation Based Fracture Mechanics (World Scientific, 1996).

32 Li, X., Wei, Y., Lu, L., Lu, K. & Gao, H. Dislocation nucleation governed softening and maximum strength in nano-twinned metals. *Nature* **464**, 877-880, (2010).

33 Caillard, D. & Martin, J. Thermally Activated Mechanisms in Crystal Plasticity (Pergamon, 2003).

34 Sheppard, D., Xiao, P., Chemelewski, W., Johnson, D. D. & Henkelman, G. A generalized solid-state nudged elastic band method. *The Journal of Chemical Physics* **136**, 074103, (2012).

35 Ago, H. *et al.* Science of 2.5 dimensional materials: paradigm shift of materials science toward future social innovation. *Science and Technology of Advanced Materials* **23**, 275-299, (2022).

36 Park, J. M., Cao, Y., Watanabe, K., Taniguchi, T. & Jarillo-Herrero, P. Tunable strongly coupled superconductivity in magic-angle twisted trilayer graphene. *Nature* **590**, 249-255, (2021).

37 Hod, O., Meyer, E., Zheng, Q. & Urbakh, M. Structural superlubricity and ultralow friction across the length scales. *Nature* **563**, 485-492, (2018).

38 Liu, K. *et al.* Evolution of interlayer coupling in twisted molybdenum disulfide bilayers. *Nature Communications* **5**, 4966, (2014).

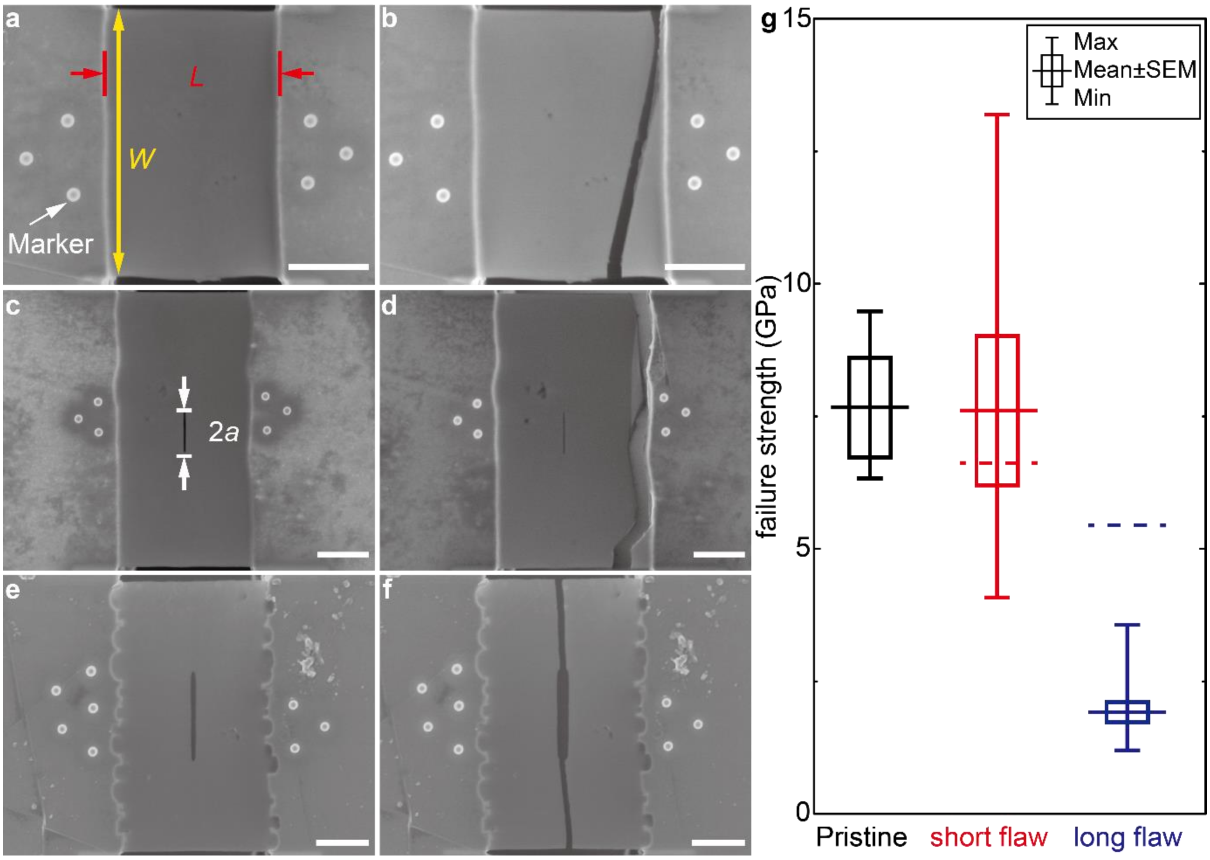

Fig. 1. *In-situ* quantitative tensile tests of MBN. (**a**) Suspended MBN without pre-crack before a tensile test, and (**b**) after a tensile test; (**c**) Flaw insensitivity observed in a suspended MBN with a short pre-crack before a tensile test, and (**d**) after a tensile test; (**e**) Flaw sensitivity observed in a suspended MBN with a long pre-crack before a tensile test, and (**f**) after a tensile test; (**g**) The failure strength of measured MBN strip. Data are presented as mean values +/- SEM, and error bars indicate the range (minima to maxima) of the data ($n_{\text{prisitne}} = 3$, $n_{\text{short flaw}} = 6$, and $n_{\text{long flaw}} = 13$). Dashed line is the mean of predicted FI strength. Scale bars: 1 μm for (**a**), (**b**), (**c**), (**d**), (**e**), and (**f**).

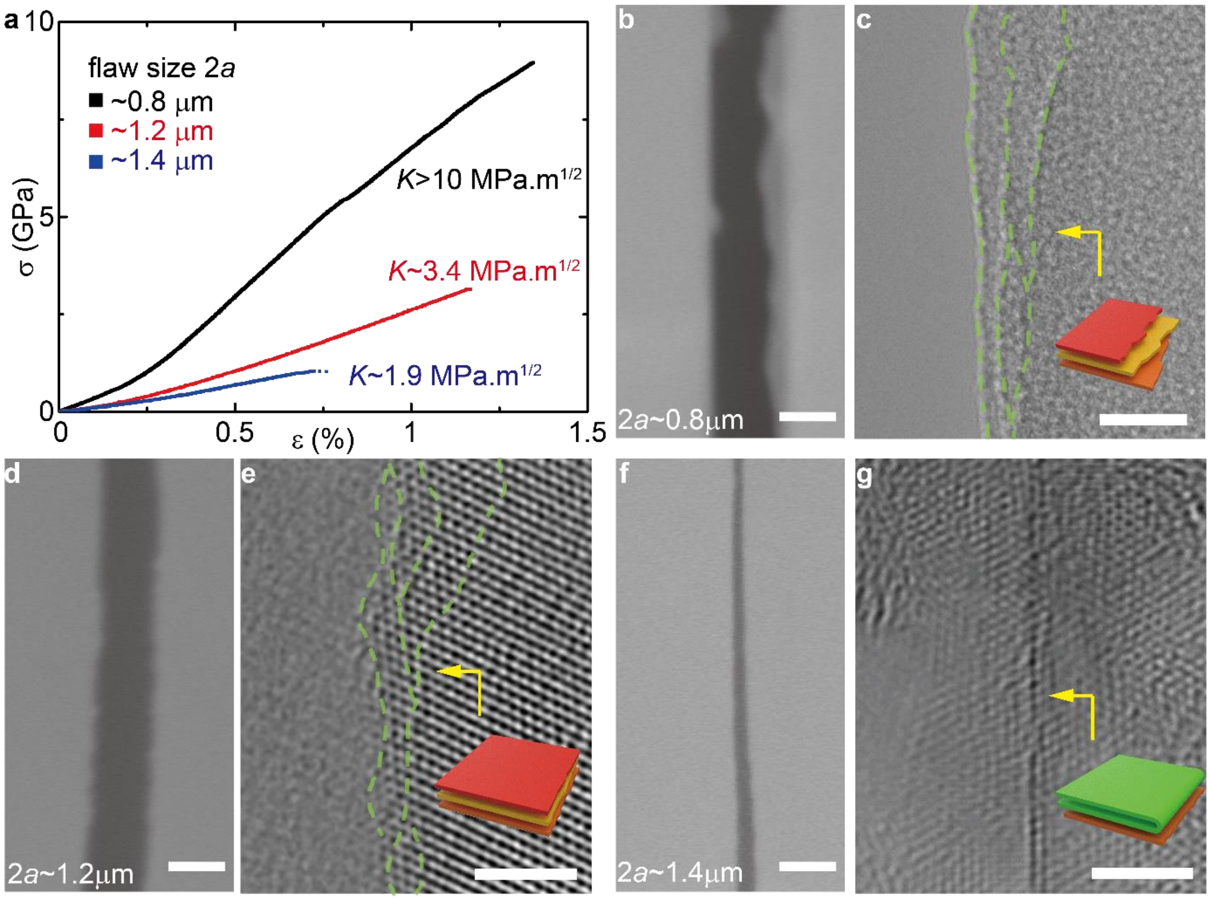

Fig. 2. MBN crack edge characterization after tensile testing. (**a**) Stress-strain curves of three typical MBN with flaw size $2a$ = ~0.8 μm, ~1.2 μm and ~1.4 μm; (**b**) SEM image of an asynchronous crack edge of a fractured MBN with pre-crack length of ~0.8 μm and estimated fracture toughness above 10 MPa.m$^{1/2}$; (**c**) TEM images of the rough crack edge, where the insert in **(c)** shows a schematic of the asynchronous fracture edge; (**d**) SEM image of a straight crack edge of a fractured MBN with pre-crack length of ~1.2 μm and fracture toughness around 3.4 MPa.m$^{1/2}$; (**e**) TEM images of the rough crack edge at atomic scale, where the insert in (**e**) shows a schematic of the transition from asynchronous to synchronous fracture edges; (**f**) SEM image of a fractured MBN with pre-crack length of ~1.4 μm and fracture toughness around 1.9 MPa.m$^{1/2}$; (**g**) TEM images of atomically smooth crack edge, where the insert in **(g)** shows a schematic of the synchronous fracture edge. Scale bars: 100 nm for (**b**), (**d**), and (**f**); 20 nm for (**c**); 2 nm for (**e**) and (**g**).

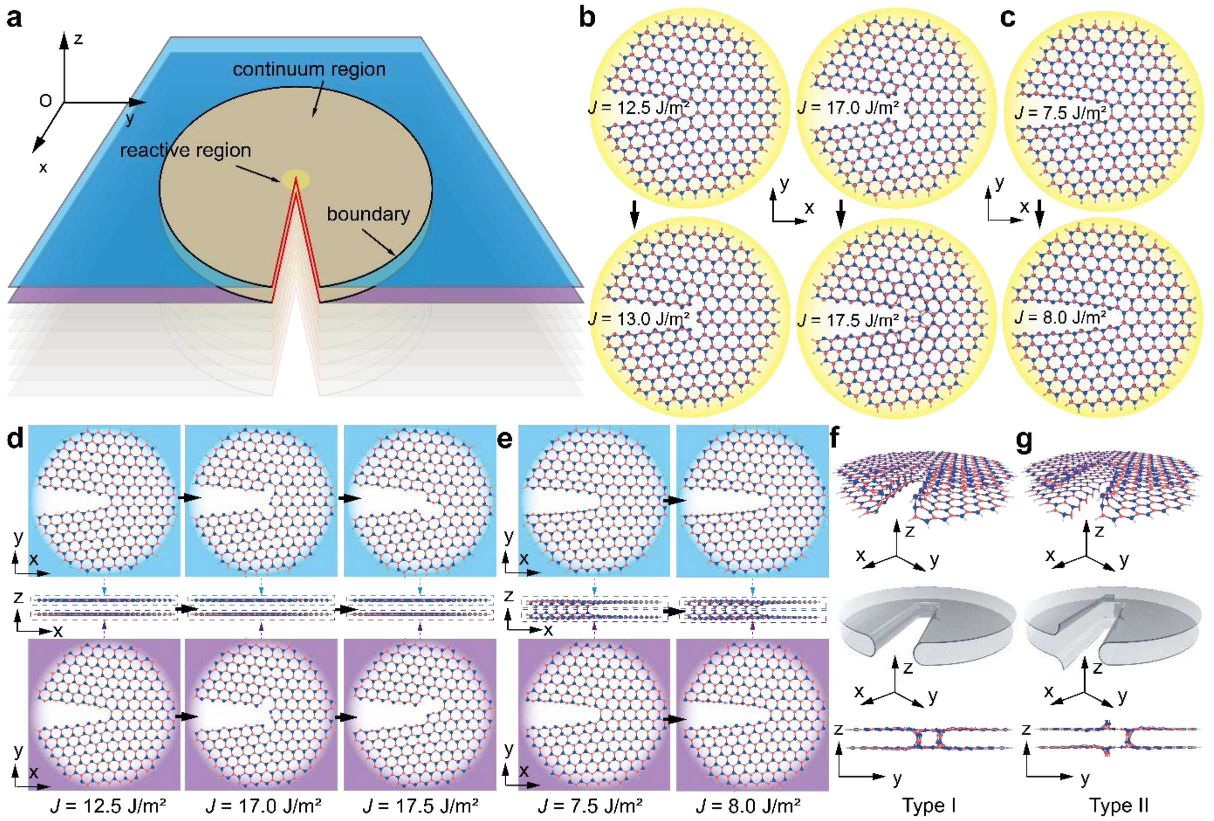

Fig. 3. Ideal K_I field analysis of dual fracture modes in MBN. (**a**) Multiscale schematic of crack initiation in MBN; (**b**) Sequential critical events of crack growth initiation in non-reconstructed MBN; (**c**) Critical events of crack growth initiation in reconstructed MBN; (**d**) Sequential critical events of crack growth initiation in adjacent layers of non-reconstructed MBN; The top and bottom layers shown are highlighted by the blue and purple backgrounds. (**e**) Critical events of crack growth initiation in adjacent layers of reconstructed MBN; The top and bottom layers shown are highlighted by the blue and purple backgrounds. (**f**) Type I edge reconstruction in MBN; (**g**) Type II edge reconstruction in MBN.

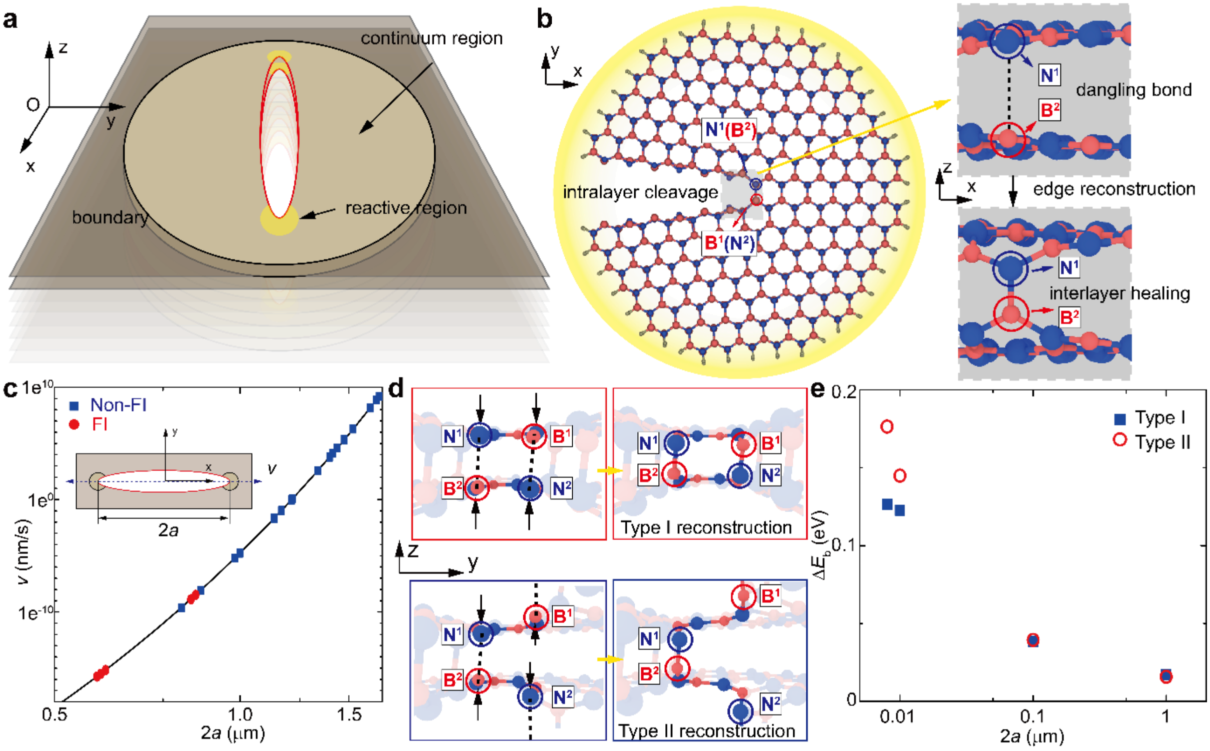

Fig. 4. Flaw-size dependence of fracture modes in MBN. (**a**) Multiscale schematic illustration of crack propagation in MBN with a central crack; (**b**) Sequential critical events of crack growth initiation in reconstructed MBN (from intralayer cleavage to interlayer healing); (**c**) Theoretical prediction of the relationship between the mobility v of reconstructed crack tip and the flaw size $2a$; (**d**) Interlayer healing transition in type I and type II reconstructed MBN; (**e**) Relationship between the reconstructed energy barrier ΔE_b and the flaw size $2a$.

Methods

MBN testing sample preparation. MBN nanosheet was mechanical exfoliated from a bulk *h*-BN crystals synthesized by the high-pressure and high-temperature method using wafer tape (Nitto Denko), and was deposited on a clean SiO_2/Si substrate (UniversityWafer). PMMA (MicroChem, A4) was spin-coated on the sample substrate and then lifted off from the substrate using NaOH solution (Sigma-Aldrich). The PMMA/*h*-BN thin film was further transfer to the copper glider Aperture Grids (Ted Pella). A probe station and a micromanipulator (Micromanipulator) were used to dry transfer the target MBN sample to the Rice push-to-pull (PTP) device (**Supplementary Section 1**). Then the PMMA layer was removed through annealing method in a vacuum tube furnace (MTI corporation, OTF-1200X). After the annealing process, the samples were carefully screened using SEM for subsequent tests.

In-situ SEM mechanical testing. *In-situ* mechanical test was carried out in a SEM/FIB (FEI, Helios Nanolab 660) equipped with an in-SEM nanoindentation system (Bruker PI-85L). The PTP device with the MBN sample loaded on it was fixed on the sample holder using the SEM sample mounting hard wax (Ted Pella) and a small amount of silver paste (Electron Microscopy Sciences). Before the mechanical test, FIB was used to define the testing geometry and manufacture the pre-crack. Then, the nanoindenter tip would push the top beam of the device, which converts the compression force to the uniaxial tensile force applied to the samples. The nano-indenter tip was controlled to move at a speed of $10\ \mathrm{nm \cdot s^{-1}}$. The quantitative nanoindentation system recorded the force and displacement of the tip and the deformation and fracture process were recorded by the SEM system for further analysis and digital image correlation (**Supplementary Section 1**). Atomic force microscopy (Park, NX20) was used precisely measure the thickness of the tested MBN sample. The methods used to calculate measured stress σ_m, strain ε_m, stress intensity factor K and typical results can be found in **Supplementary Section 1, Fig. S2 and Table S1**.

TEM tests and simulation. After mechanical test, fractured MBN samples on PTP were directly loaded in the TEM (FEI, Titan). High-resolution transmission electron microscopy (HRTEM) images are performed with a double-corrected Titan cubed Themis G2 operated at 300 kV. The microscope is equipped with a Ceta camera, a Gatan Quantum 966 energy filter and an electron monochromator. QSTEM code [39] was used to simulate the TEM images of bilayer h-BN with closed and open edges. Under an accelerating voltage of 300 kV, a spherical aberration coefficient (Cs) of 0.001 mm, and Scherzer defocus condition, the double layer h-

BN sheets could be treated as weak-phase objects, and intensity of TEM images are proportional to the atomic potential and phase of electron exit waves. The simulated HRTEM images were further used to compare with the experimental results. Details can be found in **Supplementary Section 1**.

DFT calculation and vdW correction. For an accurate description of structural evolution in *h*-BN, spin-polarized electronic structure optimizations based on the density functional theory (DFT) are carried out by Vienna Ab-inito Simulation Package (VASP) [40,41]. The generalized gradient approximation (GGA) in the Perdew Burke Ernzerhof (PBE) version is utilized for the exchange-correlation functional [42,43]. To avoid the artificial interactions between the 2D sheet and its periodic images, vacuum space larger than 10 Å is included in the non-periodic direction. Several vdW schemes have been chosen to calibrate the interlayer interaction of MBN as shown in **Table S2**. The vdW-D4 is selected for all MBN calculations as the predicted interlayer distance is the closest to experiment [44,45].

Evaluating the reconstructed energy barrier. The generalized solid-state nudged elastic band (G-SSNEB) is used to evaluate the energy barrier of interlayer healing aligned with corresponding cell volume change in z dimension (out-of-plane direction with periodic boundary condition), which is widely adopted in exploring the energy barrier of phase transitions in small system [34]. In the *ab initio* G-SSNEB calculations, the initial state is chosen as the optimized crack tip configuration before intralayer cleavage, while the final state is defined as the optimized crack tip configuration after interlayer healing. Both of them have been optimized by conjugate gradient (CG) method. The stress tensor section in the VTST code[46,47] has been modified in aim to only allow the volume change in z direction during the exploration of energy landscape.

Data Availability

The data and code that support the findings of this study are available from the corresponding authors on reasonable request.

References

39 Koch, C. T. Determination of core structure periodicity and point defect density along dislocations. *Ph.D. Thesis*, (2002).

40 Kresse, G. & Furthmuller, J. Efficiency of ab-initio total energy calculations for metals and semiconductors using a plane-wave basis set. *Comp Mater Sci* **6**, 15-50 (1996).

41 Kresse, G. & Furthmuller, J. Efficient iterative schemes for ab initio total-energy calculations using a plane-wave basis set. *Phys Rev B* **54**, 11169-11186 (1996).

42 Kresse, G. & Joubert, D. From ultrasoft pseudopotentials to the projector augmented-wave method. *Phys Rev B* **59**, 1758-1775 (1999).

43 Perdew, J. P., Burke, K. & Ernzerhof, M. Generalized gradient approximation made simple. *Phys Rev Lett* **77**, 3865-3868 (1996).

44 Kim, S. M. *et al.* Synthesis of large-area multilayer hexagonal boron nitride for high material performance. *Nature Communications* **6**, 8662, (2015).

45 Pease, R. S. An X-ray study of boron nitride. *Acta Crystallographica* **5**, 356-361, (1952).

46 Henkelman, G., Uberuaga, B. P. & Jónsson, H. A climbing image nudged elastic band method for finding saddle points and minimum energy paths. *The Journal of Chemical Physics* **113**, 9901-9904, (2000).

47 Henkelman, G. & Jónsson, H. Improved tangent estimate in the nudged elastic band method for finding minimum energy paths and saddle points. *The Journal of Chemical Physics* **113**, 9978-9985, (2000).